Radio analysis of Galactic Star Formation Regions

using data from the Giant Meterwave Radio Telescope

A. Iyer, A.K. Dubey, C. Talegaonkar, R.N. Reddy

Astronomy NIUS Camp, Indian Institute of Space Science and Technology,
Thiruvananthapuram, India
e-mail: rnr1410@gmail.com, chinmay0301@gmail.com

December 20, 2017

ABSTRACT

Aims. IRAS 16164-5046 is an infrared source in the massive star forming region RCW106. In this project, we tried to investigate the data collected by observing the source at 610 MHz and 1280 MHz by the GMRT, Pune, India to search for any non-thermal regions near the source.
Methods. AIPS was used for data reduction and forming the image of the source. By generating the spectral index map of the region using the images in 610 MHz and 1280 MHz, based on the obtained values of spectral indices (α), we tried looking for non-thermal emissions in the region, and try to find and understand their sources.
Results. Obtained spectral index maps after data reduction using AIPS for the region of interest at 610 MHz and 1280 MHz. Estimated the magnetic field for the a given region, and also proposed the further studies of a supernova remnant observed in the field of view of the image

1. Introduction

Stars are formed deep inside molecular clouds, where matter starts accreting onto a central mass gravitationally, leading to the formation of what is known as a *Young Stellar Object (YSO)*. One of the most striking features of this phase is the ejection of matter at large velocities perpendicular to the accretion disk, into the enveloping molecular cloud, inside which it is formed. This process is believed to occur due to the need to disperse angular momentum from the vicinity of the *YSO* to the outer regions. This drives large scale outflows seen over the entire stellar mass spectrum. Jets and outflows are suspected to drive turbulence in molecular clouds, and hence cause star formation in the vicinity [1]. In case of massive *YSO*'s, which are deeply embedded inside a molecular cloud, they can either lead to, or halt the infall process [2]. The magnetic field, according to numerical estimates, plays a very prominent role in the generation of jets [3][4][5]. The regions from which the jets are launched have been studied using high resolution spectroscopy in optical bands for a better understanding of the base velocity structure [6].

Radio investigation of jets have been far fewer than optical or infrared, due to the weakness of the signal, being in the order of a few *mJy*. Radio emissions are believed to originate, either from

1. partially ionised jets consisting of material ejected from the source (typically close to the source, 10 to 100 AU) [9]
2. shock fronts at the edge of outflows, where the supersonic velocity gas collides with the material of the surrounding molecular cloud. This forms Herbig-Haro (HH) objects [10]

Radio emissions from Synchrotron emission occurs when the electrons are accelerated to relativistic velocities. Since the jet velocity from a *YSO* is of the order of a few $100km/s$, it is the shock at the meeting point of the jet and the surrounding cloud where the particles, due to diffusive shock acceleration (DSA), by Fermi 1 Type mechanism, which accelerates the particles to the velocities that give rise to synchroton radiation. [20]

Most radio detections have been done for low mass YSOs with HH objects in the vicinity [11]. A tentative detection of non thermal radiation from a low mass protostar was carried out on DG Tau [12]. Observation of high mass YSOs in radio frequencies, is usually rare, (though a handful have been detected, [13][14] due to their rarity, distance, and very short lifetimes. The first confirmed detection of non thermal emissions in radio was for the massive protostellar object, IRAS 18162 -2048 [15] Radio emissions from YSOs are typically thermal, caused by free-free emissions from the shock front, and that is the primary reason why non thermal emissions in radio had not been detected until recently.

Spectral indices greater than 0.1 are associated with thermal emissions [16], while spectral indices lesser than -0.5 are usually associated with non thermal emissions [17]. At lower frequencies, spectral indices can play a very significant role in helping detect non thermal emissions [18][**?**] due to the fact that thermal free-free emissions are supposed to be negligible at these frequencies (optically thick). Since the slopes have opposite signs, the spectral index for regions with both non thermal emissions and optically thick thermal emissions flatten out, depending upon the contribution of the two processes. [19]. All these findings motivated us to look at the IRAS 16164 -5046 region, in the 610 MHz band.

2. GMRT observations and Data reduction

2.1. Data Reduction using AIPS

Radio observations have been carried out with data from the Giant Meterwave Radio Telescope (GMRT), Pune, India, under two frequency bands- 610 MHz and 1280 MHz, both having a bandwith of 16 MHz. The GMRT is a collection of 30 antennae, each of diameter 45 m, with baselines ranging from 105 m to 25 km, enabling us to view both small scale and large scale structures. The radio source 3C286 was used as the flux clibrator, while sources 1714-252 and 1830-360 were used as phase calibrators for the 610 MHz observation. 1626-298 and 3C286 were used as the phase and flux calibrators for the observations at 1280 MHz. The right ascension and declinations of the above mentioned sources can be obtained from the GMRT observer manual.

Obs. Band	Resolution	σ	Field of view
610 MHz	1.86"× 1.86"	0.0048	0.6°
1280 MHz	0.7" × 0.7"	0.00205	0.286°

Parameters for 610 MHz and 1280 MHz

Data reduction was carried out using the NRAO Astronomical Image Processing System (AIPS). Corrupted data due to radio frequency interference, bad antennae, bad baselines, etc. was flagged using UVPLT, TVFLG and UVFLG. The flux and phase calibrators were cleaned followed by calibrating the source with the generated FG tables corresponding to the flux and phase calibrators.

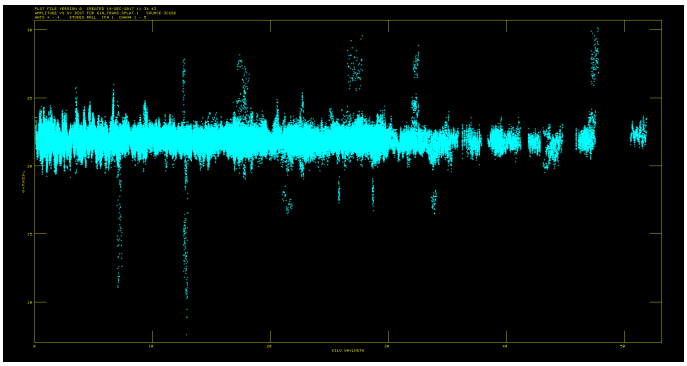

Fig. 1: u-v plot of 3C286 (flux cal) before cleaning

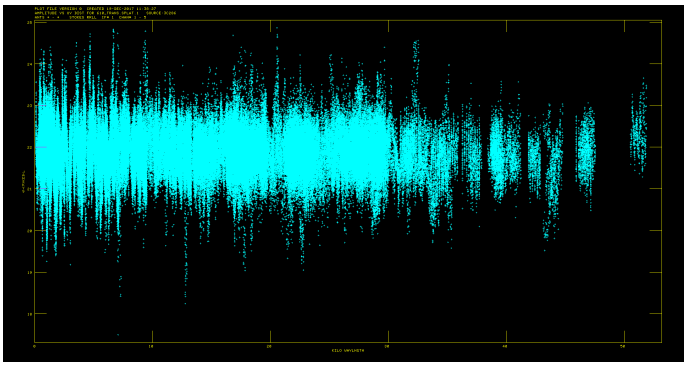

Fig. 2: u-v plot of 3C286 (flux cal) after cleaning

The images above Fig. 1 and Fig. 2 show the difference in the UV plot of the flux calibrator before and after cleaning the data for 3C286. The target image was then calibrated manually as well as by multiple rounds of cleaning by self-calibration to remove phase and amplitude errors. The task SNPLT was used to see erreneous phase errors in the images obtained while calibration. The data was then once again cleaned and deconvolved using the task IMAGR after the final calibration. Since the region of interest lies in the galactic plane, a correction for the contribution of the galactic plane, to the system temperature [7] was applied. This correction is particulary significant at low frequencies.

The fluxes at both the wavelengths are scaled by a correction factor $(T_{sys} + T_{gal})/T_{sys}$. T_{sys} is the system temperature corresponding to the flux calibrators obtained from the GMRT observer manual. T_{gal} is the temperature of the galaxy as observed in that frequency. We used the sky survey of Haslam [8] at 408 MHz. We then used the power law relation in flux to frequency (ν) and took the spectral index $\alpha = -2.6$ to estimate the T_{gal} corresponding to each frequency band. The correction factors were obtained as 2.8 and 1.36 for the 610 MHz and 1280 MHz respectively, which demonstrates the importance of this correction factor for lower frequencies.

The flux scaled images were then flattened, joining all the different parts of the image given the imager using the task FLATN. The flattened file was then corrected for beam size of the GMRT telescope, using the task PBCOR. The beam size after beam correction applied to both the images was obtained to be 14.43 " × 5.52", which when multiplied by a correction factor of 1.13 (due to FWHM considerations for a gaussian response), gives the effective beam area to be 90.4 arcsec^2. The parameters corresponding to the task PBCOR were obtained from the GMRT observer manual.

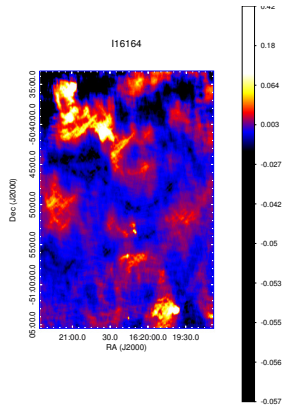

Fig. 3: IRAS16164-5046 at 610 MHz with surrounding IRAS regions

2.2. Generating the spectral index map

The image obtained at 1280 MHz was adjusted for the resolution corresponding to the 610 MHz image, by the selecting the same u-v range for both the frequency bands, by using the cell size and beam parameters of the 610 MHz data in the SETFC task while processing the .SPLIT file corresponding to the 1280 MHz. The final flux scaled and beam corrected images at the same resolutions for both the bands were corrected for the linear shift using ds9. Loading the images in R and G frames in ds9, the shift in the pixels in arcseconds in both X and Y directions was obtained. The OGEOM task was then used to realign the 610 MHz image

by the corresponding shifts. This gives the 2 re-gridded images at the same resolution, which can be used to map the spectral index of the region of interest. The 2 images were aligned using the peak value of the central source, but there are visible shifts in the diffuse regions in the outer regions due phase errors. Hence, we provide a rough estimate of the spectral index for outer IRAS sources by integrating fluxes for corresponding areas in the 2 images. Fig. 3 shows the central part of the source IRAS16164-5046 along with neighbouring IRAS regions. The image was generated using AIPS, with an appropriate constrast applied through ds9. The task COMB was used to generate spectral index maps. The spectral index (α) is defined as $S_\nu \propto \nu^\alpha$, where S_ν is the flux density at frequency ν. We considered pixels with flux larger than 3σ in both the images, where σ is the rms of the corresponding image, and is reported for the corresponding bands in Table 1.

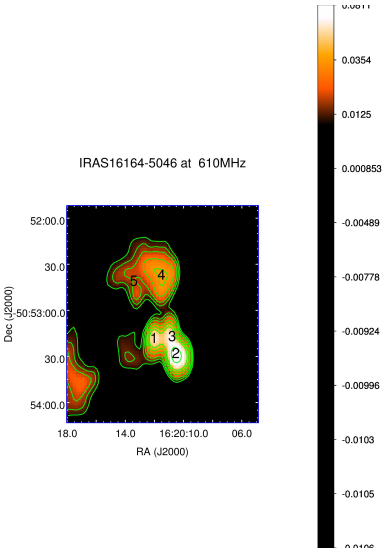

Fig. 4: IRAS16164-5046 central region at 610 Mhz

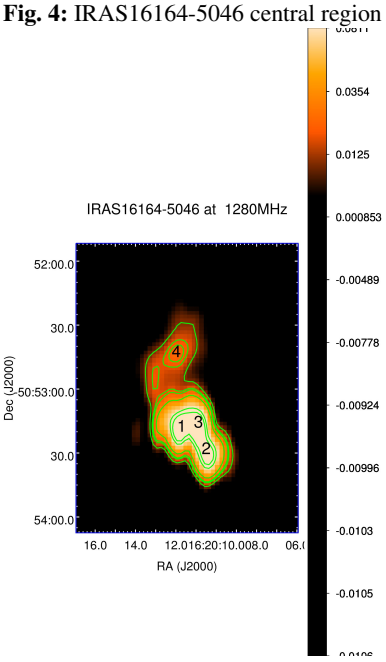

Fig. 5: IRAS16164-5046 central region at 1280 MHz

The above Fig. 4 shows the central region, i.e. the IRAS16164-5046 region. We have marked 5 regions which could be spotted distinctly in the 610 MHz image. The corresponding image for the 1280 MHz is also shown above (Fig. 5). The region 5 corresponding to 1280 MHz image is quite noisy, hence is not taken in consideration for finding spectral index of that region. The spectral index maps for the central regions with appropriate error bars were calculated using the COMB task in AIPS. We observed negative values of α in the region 4 in 610 MHz, i.e. in the bow-shock above the central source.

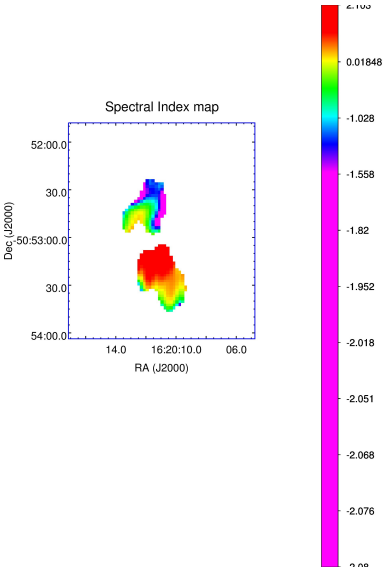

Fig. 6: spectral index map of IRAS16164-5046

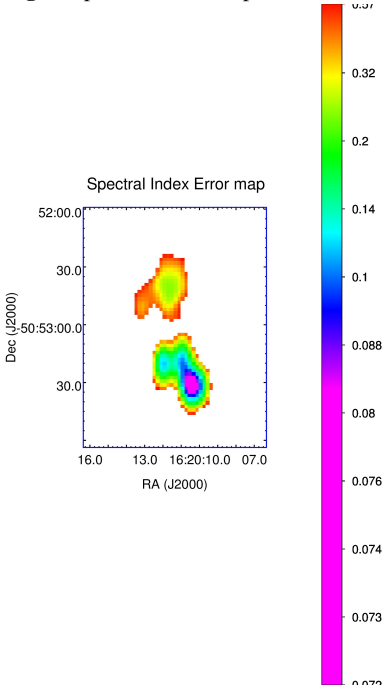

Fig. 7: Corresponding error map

3. Discussion and Results

3.1. Magnetic field estimations

The negative spectral index observed in the shock-wave can be attributed to a non-thermal synchroton radiation in the region as discussed above. Using the conventional method of minimising the total energy of the synchrotron source leads to the approximate equipartition of energy between magnetic field and

the relativistic particles. The standard energy distribution of electrons in the synchroton emission depends on the energy as $N(E)dE \propto E^{-\delta}dE$ where $N(E)$ is the standard energy distibution, $\delta = 1 - 2\alpha$ is the power factor. For an elliptical region of non-thermal radio emissions of angular dimensions $\theta_x \times \theta_y$, the magnetic field from equipartition B_{eq} is [21]:

$$\left(\frac{B_{eq}}{gauss}\right) = 5.69\times10^{-5}\left[\frac{1+K}{\eta(sin\phi)^{\frac{3}{2}}(\alpha+\frac{1}{2})}\frac{arcsec^2}{\theta_x\theta_y}\right]^{\frac{2}{7}}\left[\left(\frac{Kpc}{s}\right)\left(\frac{F_0}{Jy}\right)\frac{\nu_2^{\alpha+\frac{1}{2}}-\nu_1^{\alpha+\frac{1}{2}}}{\nu_0^{\alpha}(\alpha+\frac{1}{2})}\right]^{\frac{2}{7}} \quad (1)$$

where

K	Energy ratio of heavier ions and electrons
η	beam filling factor
ϕ	angle between magnetic field and line of sight
α	spectral index
s	path length through the line of sight
F_0	radio flux density at ν_0
ν_1, ν_2	cut-off frequencies

It is to be noted that the above formula has inherent approximations for the values of the necessary parameters. For our calculations, we have approximated the parameters as follows -:

1. K is approximated to energy ratio of protons to electrons, with value ~ 30 [22]. Value of K is between $20 - 40$, leading to a 10% error.
2. s is roughly the width of the emitting region in sky. From inspection of infrared overlay on radio image, $\eta \sim 1$.
3. $\phi \approx 28$ which is evaluated assuming magnetic field to be perpendicular to the accretion disk [23] . The value of ϕ has significant uncertainties, as indicated by the literature survey.
4. For GMRT observations at $\nu_0 = 0.610$ GHz, we take cutoff frequencies at 0.01 GHz and 100 GHz.
5. The value of η is as of now a very crude estimate. It is expected to be be less than unity, due to clumpiness in the bow shock region.

After taking into account all the above stated approximations, we get $B_{eq} \approx 0.63\ mG$. So it is of the same order of magnitude as expected, i.e. of the order of mG [24]

3.2. Spectral Index mapping and calculations

The spectral index (α) estimation helps in confirming the nature of radiation (thermal or non-thermal) for a given region. After reducing the data and generating spectral index map and spectral index error map for the field, objects were identified and their total spectral index with error was obtained. The results are give in the follwing table.

Region	$\alpha \pm \delta\alpha$	area
1	1.1019195 ±0.18820636	172.98001
2	0.19543553 ±0.13261445	307.90442
3	1.3310384 ±0.21740613	138.38401
4	-0.84786036 ±0.1995158	96.868806

Area($arcsec^2$) and Spectral Index values

It is known that an α of 0.5 or less suggests a non-thermal emission in a region. From the table, we can see that source 4 is showing an $\alpha \sim -0.85$ suggesting a non-thermal radio emission in the source.

3.3. Diffusive Shock Acceleration

As mentioned in the introduction, the acceleration of the particles from the jet (400 km/s) to relativistic velocities is theorised to occur by Diffusive Shock Acceleration at the point where the jet terminates [25].
Here, we give a qualitative picture of the process.
Also known as the “Fermi Type 1 Mechanism”, it is a process where charged particles gain energy while systematically crossing a shock front. This rapid back and forth motion across the shock front requires the presence of magnetic fluctuations that change the angle between the particle’s velocity and the mean magnetic field. [25][26].
The term "First order" comes from the fact that the energy gain per shock crossing is proportional to β_s, the velocity of the shock divided by the speed of light.

This phenomena also explains the presence of the non thermal radiation in our source 4.

3.4. Overlaying radio bow shock on the infrared image

The radio image was superimposed on the 8 μm infrared image. This was done as the 8 8 μm band is sensitive to emission from PAH (Polycyclic Aromatic Hydrocarbons) excited vibrationally by non ionizing photons, and the analysis of which is one of the principal methods of detecting bow shocks [27].

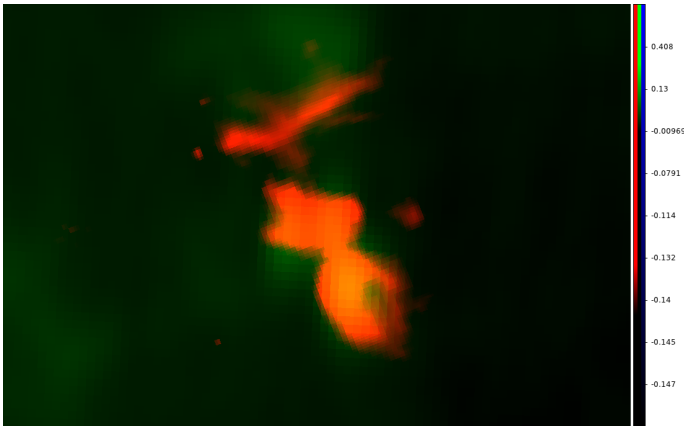

Fig. 8: Overlay image of 8 μm infrared band image (red) over 610 MHz Radio bandwidth (green)

As seen in the image above, the 8 μm image has an excited band that exactly matches the boundary of the radio detected bow shock on the side of the expected YSO. This provides more evidence for the theorised presence of the non thermal, radio bow shock.

3.5. Detection of other objects

A supernova remnant SNR G332.4-00.4 was also detected in the field of view in the 610 MHz image, but no further analysis was done due to large errors caused by its large angular distance from the center of the field. The antenna response away from the centre causes the errors at the edges of the field. It was not detected in the 1280 MHz image due to its smaller field of view. This confirmation, that it can be observed at our bands, can lead to further studies of the object at radio frequencies. An extensive literature survey and archive study needs to be done regarding this, before proceeding further for this object.

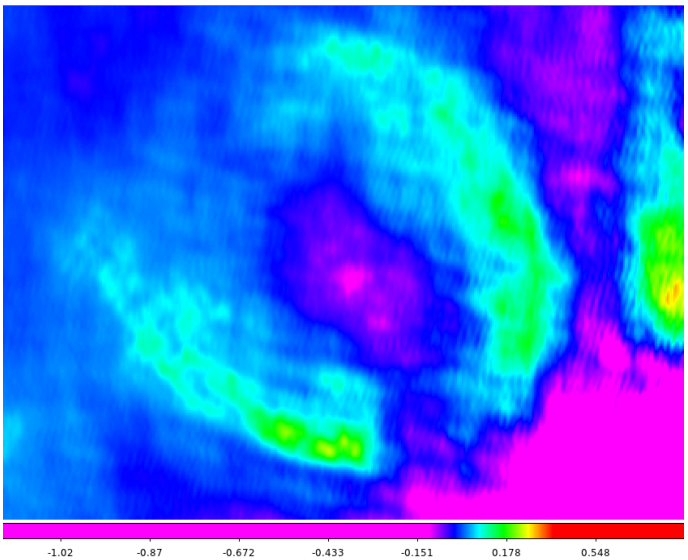

Fig. 9: The supernova remnant SNR G332.4 -00.4 in 610MHz band width

4. Summary

After a proper data reduction of the 610 MHz data using AIPS, we obtained an image, which was further beam corrected and rescaled for taking into account the difference of temperature in the galactic plane and the system temprature of the flux calibrator. This led us to obtaining the final image at 610 MHz. A similar process was again done for the 1280 MHz data by Group 1 using the beam area and cell size corresponding to 610 MHz. These low frequency Radio observations of the region at 610 MHz and 1280 MHz with the subsequent spectral index mapping, helps us conclude about the dominant non thermal radiation at the bow shock like region visible in the radio spectrum. The radio image was superimposed on the 8 μm band, which confirmed the presence of a bow shock at that position. This bow shock was theorised to be formed from the interaction of jets from one or more YSOs in the central region with the surrounding cloud. The existence of the synchrotron radiation helped us calculate the magnetic field of the region, which is of the order of 0.63 mG.

5. Acknowledgement

We would like to thank Veena Ma'am and Dinil Sir for their full fledged help in helping us with Theoretical Astrphysics and the AIPS software. We are indebted to Prof. Sarita Vig and Prof. Anandmayee Tej for guiding us with the literature survey and giving suggestions like calculating magnetic field for the non-thermal region, infrared overlaying etc. We would also like to thank Vedant et al., 2017 for generating the map at our resolution for the 1280 MHz data. Last but not the least, we would like to thank Dr. Aniket Sule, and Dr. Pritesh Randive for making the camp happen in the very first place.

References

[1] Arce et al, 2004,07
[2] Frank et al, 2014
[3] Zanni et al, 2007
[4] Fendt et al, 2006
[5] Ouyed and Pudritz, 1997
[6] Coffey, Bacciotti and Podic, 2008
[7] Rao and Roy, 2004
[8] Haslam et al, 1982
[9] Anglada, 1996
[10] Rodrigues, 1989
[11] Girart et al, 2002
[12] Ainsworth, 2014
[13] Rodriguez, 2011
[14] Purser et al, 2016
[15] S Vig et al, 2017
[16] Olnon, 1975
[17] Kobulnicky and Johnson, 1999
[18] Veena et al, 2016; Nandkumar et al, 2016
[19] Rodriguez-Kamenetzky et al, 2016
[20] Padovani et al, 2015 to 2017
[21] Miley, 1890
[22] Beck and Krause, 2005
[23] Ilee,2013
[24] Crutcher, 1999
[25] Drury, 1983
[26] Kirk, 1994
[27] Kobulnicky, 2009
[28] Veena et al, 2016
[29] Nandkumar et al, 2016